Cement and Concrete Research 41 (2011) 828–841

Contents lists available at ScienceDirect

Cement and Concrete Research

journal homepage: http://ees.elsevier.com/CEMCON/default.asp

Modelling of isothermal coupled moisture–ion transport in cementitious materials

V. Baroghel-Bouny *, M. Thiéry, X. Wang

Paris-Est University, French Institute of Science and Technology for Transport, Development and Networks (Ifsttar former-LCPC), Materials Department, Paris, France

ARTICLE INFO

Article history:
Received 31 August 2010
Accepted 1 April 2011

Keywords:
Multiionic transport (C)
Kinetics (A)
Moisture (A)
Modelling (E)
Profile (C)

ABSTRACT

A numerical model has been developed to predict isothermal coupled moisture–ion transport in cementitious materials. Ionic transport is described by the extended *Nernst–Planck* equation, which accounts for advection of the liquid phase. Moisture transport includes Fickian water-vapour relative diffusion and Darcian liquid-phase movement. The ion effect on liquid/vapour water equilibrium is taken into account. The variations of the transport properties *vs* the degree of saturation are described by integral functions or analytical formulas. A *Freundlich's* type description along with instantaneous *Friedel's* salt formation is considered for chloride binding at equilibrium. A kinetic equation is added in the cases of non-instantaneous binding processes. The governing equations, as well as the methods of assessment of the material properties required as input data, are described in the paper. Moreover, examples of application of the model in lab conditions are provided, which highlight its capability of predicting moisture/ionic concentration profiles even in complex configurations.

1. Introduction

Chloride-induced reinforcement corrosion is the major cause of premature damage in reinforced concrete (RC) structures located in marine, coastal or road environments [1,2]. Various mechanisms may occur simultaneously depending on the environmental conditions and on the material. In saturated conditions (*e.g.* permanent immersion in seawater), chlorides from the environment penetrate into the covercrete by a coupled diffusion-binding process. In coastal areas, in tidal zones or in the presence of deicing salts, wetting–drying cycles coupled with the effect of wind induce a non-saturated state and an inhomogeneous spatial distribution of moisture in the structure. In such non-saturated conditions, ionic transport relies on advection, in addition to diffusion. This induces a significant higher rate of chloride ingress and of reinforcement corrosion, in particular in the case of wetting–drying cycles, compared to the case of diffusion (in saturated conditions) [3–5,13]. Only in some cases (*e.g.* high-performance concretes), the impact of these cycles will be limited to the surface zone of RC elements and will have no significant effect on the chloride concentration distribution deeper in the element [24]. Besides, research works [6–8,34,35] have shown that the presence of salts in the pore system yields a decrease in the drying rate. Moreover, when a salt-contaminated concrete structure is drying, ions are transported towards the evaporation front, where they accumulate and where salts can crystallise, generating for example unaesthetic efflorescences [13].

Therefore, ionic transport in non-saturated cementitious materials involves complex chemical and physical mechanisms. A detailed knowledge of these mechanisms and a relevant implementation of the associated laws in a numerical model are essential to understand the phenomena and hence to predict accurately RC structure service life.

A lot of works have contributed to clarify the fundamental aspects of ionic transport in non-saturated concrete and numerous models have been developed, in order to predict chloride ingress in RC structures (see *e.g.* [12,14,15,26,36,37,39,47,48] and the literature reviews in Refs. [2,16]). The difficulties linked to the description of transport processes in non-saturated concrete can be related to the intrinsic complexity of the material and to the intricate nature of the phenomena. Some of these difficulties also rely on the fact that the various researchers have used different approaches to study these processes: for example differences in the state variables, in the driving forces of moisture or ionic transport or in the physical–chemical binding description can be found. In addition, even if some of the authors account for the advection process, most of them do not take into account all of the other mechanisms/processes. Moreover, movements of liquid water (involved in the advection process) and of water vapour are usually not separated. This may induce inaccuracies in the predictions for low-permeability cementitious materials when the total gas pressure cannot be considered as a constant (*i.e.* when gas pressure variations are not sufficiently rapidly dissipated) [67].

This paper deals with the analysis and simulation of coupled moisture–ion transport in isothermal conditions in cementitious materials on the basis of well-identified physical mechanisms. A multispecies transport model, which combines liquid-water, water-

---

* Corresponding author. Tel.: +33 1 40 43 51 32; fax: +33 1 40 43 54 93.
E-mail address: baroghel@lcpc.fr (V. Baroghel-Bouny).

0008-8846/$ – see front matter © 2011 Elsevier Ltd. All rights reserved.
doi:10.1016/j.cemconres.2011.04.001

vapour and ionic transports and accounts for chloride binding and chemical activity effects, will be presented. In this model, the ionic transport process involves the species Cl^-, OH^-, Na^+ and K^+, which are the main ions present in the pore solution, and is described by the extended *Nernst–Planck* equation, which accounts for electro-diffusion of ions and advection of the liquid phase. The moisture transport process includes the relative Fickian diffusion of water vapour and dry air with respect to the gas mixture, as well as the movement of the liquid phase according to extended *Darcy's* law. The ion effect on liquid/vapour water equilibrium is taken into account by including the chemical activity of liquid water into the chemical potential formula. The variations of the transport properties *vs.* the degree of saturation are described by integral functions or analytical formulas. A *Freundlich's* type description for physical adsorption onto C–S–H, along with instantaneous *Friedel's* salt formation, is considered for chloride binding at equilibrium. A kinetic equation is added to account for the delayed binding of chlorides when their velocity is high and equilibrium binding cannot be considered as instantaneously reached (case of high-rate advective transport). Methods of assessment of the material properties required as input data for the model, such as transport coefficients and fluid-matrix interaction isotherms, will be described in the paper. The model will be numerically implemented in the 1-D case, in order to understand and quantify the phenomena in complex configurations of coupled moisture–ion transport in lab conditions (*e.g.* wetting by a salt solution after strong drying, as well as wick action test). The numerical results then obtained will be compared to experimental data available in the literature, in order to test the reliability and the efficiency of the proposed model.

2. Description of the model

In this section, the proposed model and in particular the set of governing differential equations, which describe the simultaneous moisture and ionic transport in non-saturated cementitious materials, are briefly described. In the model, the transport and mass balance equations are written at the macroscale for an elementary representative volume, within the framework of a multispecies approach.

2.1. Transport equations

The transport of the liquid phase l (mixture of liquid water w and ions i) and that of the gas phase g (mixture of water vapour v and dry air a) is assumed to be governed by extended *Darcy's* law, which reads, for an isotropic partially saturated porous medium (see Eq. (1)):

$$v_\alpha = -\frac{K}{\eta_\alpha} k_{r\alpha}(S_l) \mathrm{grad}\, p_\alpha \qquad (\alpha = l \text{ or } g) \tag{1}$$

where K is the intrinsic permeability of the material (in m^2), independent of the degree of liquid saturation S_l (−), whereas v_α, p_α, η_α and $k_{r\alpha}(S_l)$ denote the *Darcy*'s velocity (in $m \cdot s^{-1}$), the total pressure (in Pa), the dynamic viscosity (in Pa·s) and the relative permeability (−) associated with phase α, respectively.

It is worth mentioning that ionic concentrations strongly influence the dynamic viscosity η_l of the pore solution [61]. The η_l variations *vs.* the chloride concentration c_{Cl-} (in mol/m^3 of solution) of the electrolyte are fitted on experimental data (see Fig. 1) by means of the extended *Jones–Dole* type equation (see Eq. (2)) [61]:

$$\frac{\eta}{\eta_0} = 1 - 6.7 \cdot 10^{-4}\sqrt{c_{Cl-}} + 5.9 \cdot 10^{-5} c_{Cl-} - 1.3 \cdot 10^{-6} c_{Cl-}^{3/2} + 5.8 \cdot 10^{-8} c_{Cl-}^2 \tag{2}$$

where η_0 is the dynamic viscosity of pure liquid water.

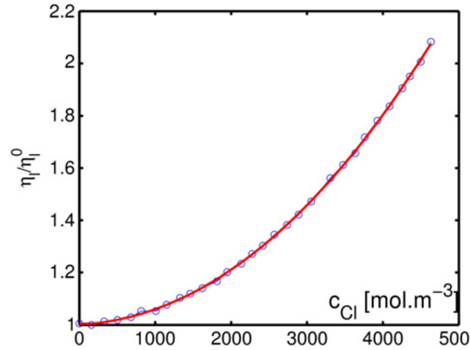

Fig. 1. Effect of chloride concentration on the relative dynamic viscosity of a solution (experimental data from Ref. [61] and fitting according to Eq. (2)).

The relative diffusion of water vapour v or dry air a with respect to the gas mixture g is assumed to be governed by *Fick's* first law, which reads (see Eq. (3)):

$$J_\alpha = -\frac{p_{atm}}{RT} f(\phi, S_l) D_{v0}\, grad\left(\frac{p_\alpha}{p_g}\right) \qquad (\alpha = a \text{ or } v) \tag{3}$$

where J_α and p_α denote the flux (in $mol \cdot m^{-2} \cdot s^{-1}$) and the partial pressure (in Pa) of constituent α, respectively, while ϕ is the porosity of the material (in $m^3 \cdot m^{-3}$), R the ideal gas constant (8.3143 $J \cdot mol^{-1} \cdot K^{-1}$), p_{atm} the atmospheric pressure (in Pa), T the absolute temperature (in K), and D_{v0} the free (out of the porous medium) water vapour diffusion coefficient in the air ($D_{v0} = 2.47 \times 10^{-5}\ m^2 \cdot s^{-1}$ between T = 20 and 25 °C). $f(\phi, S_l)$ is the so-called resistance factor, which accounts for both the tortuosity effects and the reduction of space offered to gas diffusion in a partially saturated porous medium, compared to free diffusion in the air.

Note that gas pressure is not assumed as uniform in the material and that overpressure or underpressure can thus occur during drying or wetting processes [60,67]. This implies that a non-negligible water vapour advective transport is possible through the pore network.

The transport of the various ions i present in the medium (Cl^-, OH^-, Na^+ and K^+ are addressed here) by diffusion under concentration gradient, movement under chemical activity effects and migration under the (local) electrical field, which results from the electrical interactions between ions, is described by the *Nernst–Planck* equation (see Eq. (4)) on the basis of the works reported for example in Refs. [4,19–21,25,38], but here the effective ionic diffusion coefficients D_i (in $m^2 \cdot s^{-1}$) are a function of s_l:

$$J_i = -D_i(S_l)\left[\mathrm{grad} c_i + c_i \cdot grad(\ln \gamma_i) + \frac{z_i F}{RT} c_i \mathrm{grad}\psi\right] \tag{4}$$

where J_i, c_i, γ_i and z_i denote the flux (in $mol \cdot m^{-2} \cdot s^{-1}$), the concentration (in mol/m^3 of solution), the chemical activity coefficient (−) and the valence number (−) associated with each ion i, respectively. F is the *Faraday* constant ($9.64846 \times 10^4\ C \cdot mol^{-1}$) and ψ the local electrical potential (in V).

ψ can be computed from the averaged *Poisson's* equation in non-saturated conditions [47], which relates ψ to electrical charges (see Eq. (5.1)):

$$div(S_l \tau'(S_l) \mathrm{grad}\psi) + \frac{S_l F}{\varepsilon}\left(\sum c_i z_i\right) = 0 \tag{5.1}$$

where ε is the dielectric permittivity of the liquid phase (≈10^{-10}–$10^{-11}\ F \cdot m^{-1}$) considered as equal to the relative permitivity of pure water times the vacuum permitivity, whereas $\tau'(S_l)$ is a saturation-dependent tortuosity factor (−), which reflects the connectedness of the liquid phase.

Given the very small value of ε, it can be demonstrated, on the basis of a matched asymptotic expansion, that *Poisson's* equation degenerates at the macroscale (a few mm) into the electroneutrality condition (see Eq. (5.2)) [66].

$$\sum c_i z_i = 0 \tag{5.2}$$

In saturated conditions and in the case of similar ionic concentrations as in seawater, chemical activity effects can be assumed as negligible on the basis of the results presented in Refs. [22,23] and in agreement with *Samson and Marchand* [21] who recorded a significant effect on the electrical potential but a negligible effect on concentration profiles, in the case of high ionic strengths (200–300 mol/m^{-3}). In non-saturated conditions, much higher ionic concentrations (10 times higher) can be recorded in the pore solution (S_l can reach the value of 0.1 in cases considered in Section 4). Hence, here chemical activity effects will not be considered as negligible and will be computed in the ionic fluxes as described in Ref. [28].

In the approach adopted here, the pore solution is a multispecies electrolyte, which contains ions and water molecules considered as individual species. As a result of the non-ideal behaviour of the solution, water molecule concentration can locally vary with respect to the concentration variations of the solutes. Thus, water molecules can diffuse independently. The fluid velocity v_l is chosen here as a mass-averaged velocity ($v_l = \sum E_i \cdot v_i$, where E_i is the mass fraction of each species). By definition, the diffusive molar flux J_i of each ion i (see Eq. (4)) is given by $J_i = c_i \cdot (v_i - v_l)$. Eq. (6) can hence be derived and used for the computation of the diffusive flux of water molecules J_w (in $\text{mol} \cdot \text{m}^{-2} \cdot \text{s}^{-1}$):

$$M_w J_w + \sum_{i \neq w} M_i J_i = 0 \tag{6}$$

where M_w and M_i are the molar masses (in $\text{kg} \cdot \text{mol}^{-1}$) of water w and ion i, respectively.

The mathematical description of the overall transport process of each constituent is derived by adding the advection and diffusion components (see Eq. (7)):

$$\begin{cases} w_\alpha = v_l c_\alpha + J_\alpha \ (\alpha = \text{w or i, for liquid water or ions, respectively}) \\ \text{or} \\ w_\alpha = v_g c_\alpha + J_\alpha \ (\alpha = \text{a or v, for dry air or water vapour, respectively}) \end{cases} \tag{7}$$

where w_α denotes the total flux (in $\text{mol} \cdot \text{m}^{-2} \cdot \text{s}^{-1}$) of phase α and c_α is the concentration of α (in $\text{mol} \cdot \text{m}^{-3}$), with the condition $\sum \upsilon_\alpha c_\alpha = 1$ when α = w or i, for liquid water or ions respectively, where υ_α is the molar volume of phase α in solution (in $\text{m}^{-3} \cdot \text{mol}^{-1}$). v_l and v_g are calculated by Eq. (1), whereas J_α is computed by Eqs. (3), (4) and (6) for water vapour or dry air, ions and water molecules, respectively.

2.2. Mass balance equations

The principle of the model is to solve four mole balance equations, for Cl (free and bound), Na^+, K^+ and $OH^- - H^+$. Considering $OH^- - H^+$ allows one to avoid the sink term related to water autoprotolysis. Mass balance equations associated with water vapour and liquid water are added, as well as a mass balance equation for dry air. Finally the six mass balance equations for moisture (w + v), dry air a and species j (ions or involved in solid compounds) read (see Eq. (8)):

$$\begin{cases} \dfrac{\partial}{\partial t}\left(\phi S_l c_w + \phi(1 - S_l)\dfrac{\rho_v}{M_v}\right) = -\,div\,(w_w + w_v) \\ \dfrac{\partial}{\partial t}\left(\phi(1 - S_l)\dfrac{\rho_a}{M_a}\right) = -\,div(w_a) \\ \dfrac{\partial}{\partial t}\left(\phi S_l c_j + s_j\right) = -\,div\left(w_j\right) \end{cases} \tag{8}$$

where s_j denotes the amount of ions bound onto the cement matrix (in mol/m^3 of material), which is usually expressed as a function of the concentration c_j of ions in the pore solution *via* the binding isotherm. This term is neglected here for other ions than chlorides (*i.e.* the binding of other ions is neglected during transport).

2.3. State equations and liquid–vapour water equilibrium — ion effect

The water vapour v and the dry air a are assumed to be ideal gases, as well as their mixture g. The pressure p_g is therefore the sum of water vapour and dry air pressures: $p_g = p_v + p_a$ (*Dalton's* law). The liquid pressure is governed by the capillary pressure curve equation $p_c = p_c(s_l)$, where p_c is the capillary pressure (in Pa). Therefore, the state equations read (see Eqs. (9) and (10)):

$$p_\alpha M_\alpha = RT p_\alpha \qquad (\alpha = \text{v or a}) \tag{9}$$

$$p_c = p_g - p_l = p_c(S_l). \tag{10}$$

The ion effect on the liquid/vapour water equilibrium (water-ions coupling) can be illustrated by the results presented by *Bonnet* [44] for water vapour adsorption isotherms, obtained on M1N mortar samples (see Section 3), initially saturated with various salt solutions (NaCl concentrations equal to 0, 20, 80, 160 and 314 $\text{g} \cdot \text{L}^{-1}$). As a result of a significant ion effect (in addition to the pore structure effect), for the same water content the adsorption isotherm is shifted to a lower relative humidity (RH) when the NaCl concentration increases (see Fig. 2a). This ion effect on the liquid/vapour water equilibrium is taken into account in the model by including the chemical activity of liquid water in the solution (a_w) into the chemical potential formula. This means that the chemical potential of liquid water in the solution at atmospheric pressure is equal to the chemical potential of pure water (*i.e.* in the absence of other species) added to a term, which involves a_w (*i.e.* in the presence of ions). Considering the equality of the chemical potentials of water in the vapour phase and in the liquid phase at thermodynamic equilibrium and at atmospheric pressure yields extended *Kelvin's* law (see Eq. (11)) [29]:

$$p_c = -\frac{\rho_w}{M_w} RT(\,ln h_r - ln a_w) \tag{11}$$

where $h_r = p_v / p_{vs}$ is the relative humidity (−), ranging in Eq. (11) from 0 to 1, with p_{vs} as the saturating vapour pressure of pure water at the considered temperature T (in Pa). Note that the density ρ_w (in $\text{kg} \cdot \text{m}^{-3}$) depends on ionic concentrations.

In the case of NaCl solutions, a linear empirical function of the chloride concentration was proposed in *Hedenblad's* work reported in Ref. [36] for ln a_w. Likewise, in the case of ideal (dilute) solutions, ln a_w can be simply expressed as a function of ionic concentrations. But, in the case of concentrated non-ideal solutions, a more complex description is required. Various formulas have been proposed in the literature. Here, ln a_w is expressed as a function of the ionic strength of the solution and of the chemical activities of the ions, according to the formula proposed by *Lin and Lee* in Ref. [28] on the basis of the two-ionic parameter approach developed by the authors (see [29]). This formula combines long-range interactions (according to the extended *Debye–Hückel* or *Davies* laws [21,23,47]) and short-range solvation effects (according to *Pitzer's* law [62]).

Including the capillary pressure curve equation $p_c = p_c(s_l)$ of the NaCl-free material in Eq. (11) matches the experimental adsorption data obtained in the case of M1N [44] with various NaCl contents (see Fig. 2b [29]). Therefore, the presence of ions in the pore solution does not influence the capillary pressure curve. It can thus be concluded that the capillary pressure curve is an intrinsic property of the (pore structure) of the material and that only the curve of the NaCl-free material (which is derived from the experimental water vapour sorption isotherm [29], see

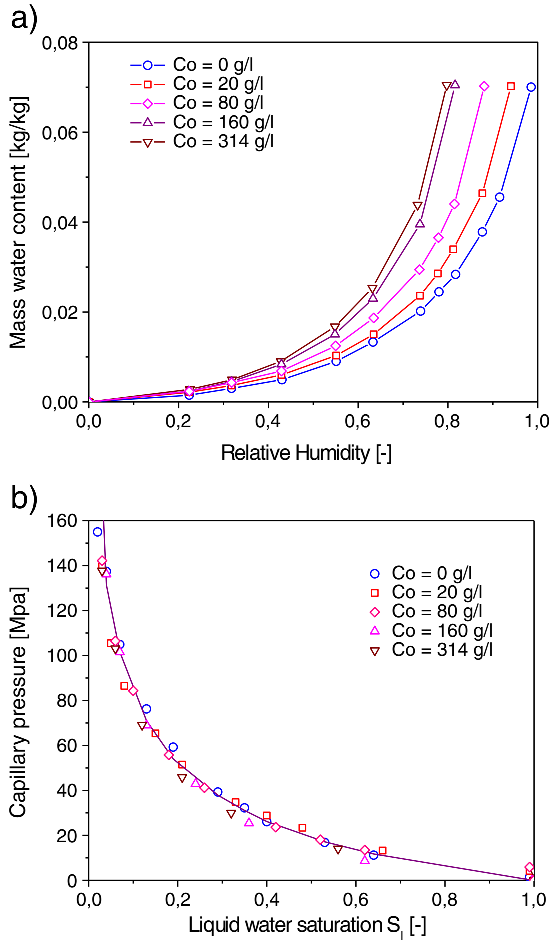

Fig. 2. Effect of the NaCl concentration c_0 on the experimental water vapour adsorption isotherm of mortar M1N (W/C = 0.50). a) Experimental water vapour adsorption isotherms [44]. b) Capillary pressure curves deduced from the experimental water vapour adsorption isotherms displayed in a).

Section 3.2) is required as input data for the model. This simplifies significantly the modelling.

2.4. Discretization and numerical treatment

To solve the complex system of non-linear equations, a numerical algorithm is needed. The six mass balance equations along with the electroneutrality condition are associated with seven primary unknown variables: Cl^-, Na^+, K^+ and OH^- concentrations, electrical potential ψ and liquid water and gas pressures. The spatial discretization of the system of equations is performed by the 1-D finite volume method. The time discretization in the transport and mass balance equations is achieved by an implicit *Euler* scheme. The system is solved by means of a standard *Newton–Raphson* algorithm [40]. Note that the proposed mathematical model adapts the timestep to the numerical stiffness of the problem.

3. Required input data and methods of assessment

Some input data are required to solve the problem, such as the transport properties of the material (*e.g.* the effective chloride diffusion coefficient and the intrinsic permeability) and the fluid-matrix interaction isotherms (*i.e.* water vapour sorption and chloride binding isotherms). As previously mentioned, the model accounts for transport property variations *vs.* s_l. Analytical laws are used as far as possible here to express such variations and to implement them easily in the numerical model.

This section is devoted to the description of the methods used to assess the required input data and to the presentation of examples of results. A normal mortar M1N (cement 1, w/c = 0.50 and s/c = 3) and a high-performance mortar M2 (cement 2, w/C = 0.53, s/c = 4.2, f/c = 0.18 and sf/c = 0.09), which includes limestone filler (f) and silica fume (sf) [4], are considered in the various examples displayed in this paper. Another normal mortar M2N (cement 2, w/C = 0.50 and s/c = 3) [4] was used, in order to illustrate chloride binding features (see Section 3.1). Both cements are CEM I. Cement 1 has a lower (C_3A) eq. content than cement 2 (10.6% and 14.6% by mass of cement, respectively, according to *Bogue's* calculations). The mortar samples have been water-cured for 90 days before testing.

3.1. Chloride binding isotherm

Various options are proposed in the model for the description (as an analytical formula) and the assessment of the non-linear chloride binding isotherm at equilibrium (see *e.g.* [5,24,31,58]). For example, physical adsorption onto C–S–H [9] according to a *Freundlich's* type description, along with instantaneous *Friedel's* salt formation [10,11], can be regarded (see Eq. (12)):

$$s_{Cl} = s^{p}_{Cl} + s^{c}_{Cl} = \mu c^{\gamma}_{Cl^-} + \delta n_{(C_3A)eq.} \tag{12}$$

where s^{p}_{Cl} and s^{c}_{Cl} are the physically and chemically bound chloride amounts (in mol/m^3 of material), respectively, μ and γ are the *Freundlich's* isotherm parameters, which vary with the binder composition, while $n_{(C3A)eq.}$ is the residual content of *equivalent* aluminates [65] of the material (in mol/m^3 of material) at the considered age. Parameter γ (positive but <1) represents the degree of non-linearity of the physical adsorption. Parameter μ stands for the capacity of physical adsorption and depends here on the C–S–H content of the material (n_{C-S-H} in mol/m^3 of material), and consequently on the mix-design as well as on the binder chemical composition [31,58]. δ is close to 2 according to stoichiometric considerations [58].

When $n_{(C3A)eq.}$ is known, *Freundlich's* isotherm parameters can be directly fitted on experimental data when available, or indirectly identified by numerical inverse analysis thanks to the proposed model (simplified by considering $S_l = 1$, which yields the multispecies transport model in saturated conditions [23,31,58]) and to an experimental total chloride concentration (tcc) profile obtained after a non-steady-state (nss) diffusion test [23,31].

Eq. (12) will be used in the examples presented in this paper (see Section 4). For mortars M1N, M2 and M2N, the μ and γ values obtained by curve fitting at the age of 90 days on the experimental data provided in Ref. [4] (obtained by the equilibrium method [32]) are reported in Table 1 (see also Fig. 3). $n_{(C3A)eq.}$ is assessed here by means of a hydration model [56] derived from the model described in Ref. [64]: $n_{(C3A)eq.} = 21$, 45 and 51 mol/m^{-3} at 90 days, for M1N, M2 (see Fig. 11b) and M2N respectively. The $n_{(C3A)eq.}$ values are small for the studied mortars, since sulphate and seawater resisting cements were used. Consequently, *Friedel*'s salt formation has a weak effect on the chloride binding isotherm (see Fig. 3).

Eq. (12) is only valid at equilibrium (for both *Friedel's* salt formation and physical adsorption). However, for example in the case of high velocity of ions through the pore network, equilibrium chloride binding is not (instantaneously) reached. Consequently, binding will be significantly reduced (hindered or delayed). Therefore, when the rate of binding is low with respect to that of transport, a kinetics equation should be used, in order to account for this delay effect [4]. Here, it is assumed that only physical adsorption is impacted by the kinetic effect, while *Friedel's* salt

Table 1
Material properties of mortars M1N, M2 and M2N.

Material property and method of assessment	M1N	M2	M2N
Apparent density of the dry material ($kg \cdot m^{-3}$) (by mercury intrusion porosimetry [4])	2220	2280	2210
Porosity accessible to water ϕ ($m^3 \cdot m^{-3}$) (by means of a hydration model [56], see Fig. 11a)	0.13	0.10	0.13
Capillary pressure curve parameters a (MPa) and m (from experimental water vapour adsorption and desorption isotherms [44])	Adsorption: $a = 11$; $m = 0.49$ Desorption: $a = 25$; $m = 0.49$	Adsorption: $a = 9$; $m = 0.49$ Desorption: $a = 24$; $m = 0.51$	Adsorption: $a = 26$; $m = 0.47$ Desorption: $a = 10$; $m = 0.49$
Freundlich's isotherm parameters μ and γ (from experimental chloride binding isotherms [4])	$\mu = 2.61$ $\gamma = 0.61$	$\mu = 3.24$ $\gamma = 0.53$	$\mu = 5.97$ $\gamma = 0.53$
Effective chloride diffusion coefficient D_{Cl-} (at $S_l = 1$) ($m^2 \cdot s^{-1}$) (by numerical inverse analysis of the experimental total chloride concentration profile provided in [4], after 7-day exposure (1) or 48-day exposure (2) to a 33-$g \cdot L^{-1}$ NaCl solution)	2.1×10^{-12} (1)	0.65×10^{-12} (2)	2.5×10^{-12} (1)
Intrinsic permeability K (m^2) (by numerical inverse analysis of drying kinetics (during exposure to RH = 4% (1) or to RH = 55% (2))	15×10^{-21}(1) 35×10^{-21}(2)	9×10^{-21}(1) 3×10^{-21}(2)	10×10^{-21}(2)

formation is assumed as instantaneous (as illustrated in Fig. 4), thus yielding Eq. (13):

$$ds^p_{Cl} / dt = -(s^p_{Cl} - \mu c^{\gamma}_{Cl-}) / \tau \qquad (13)$$

where τ is a characteristic (delay) time.

Such a description is particularly relevant in the case of short-term and high-rate advective transport (typically 24-hour wetting by a NaCl solution after drying at a very low RH, see Section 4.2).

In order to estimate the order of magnitude of the characteristic time τ, the immersion tests described in Ref. [4] have been simulated by the proposed model (which includes Eq. (13)). In these tests, crushed mortar specimens (size ≈ 3 mm) were immersed in a NaCl solution ($c^0_{Cl-ext.} = 563$ mol/m^{-3}). Since the specimens were initially almost dry (they were exposed to RH = 11% for 1 month after oven drying yielding $S^0_l \approx 0.1$, prior immersion), advection is the main chloride transport process (see Section 4) and this process is particularly rapid in this case. The evolution of the bound chloride amount *vs.* time in the M2N crushed specimen is depicted in Fig. 4. The initial jump in the curve can be attributed to instantaneous *Friedel's* salt formation [31,58], whereas the remainder (before reaching the "equilibrium binding plateau") may rather be related to the delayed physical adsorption onto C–S–H and is therefore mainly controlled by τ (wetting of the entire crushed specimen is very rapid). The value $\tau \approx 2 \times 10^4$ s is obtained by fitting simulation results on experimental data. Hence, the time required to reach equilibrium in the case of M2N is close to 2 days (see Fig. 4). The τ value is small, justifying thereby that in most of cases the kinetic effect is neglected.

3.2. Capillary pressure curve

Capillary pressure curve data are derived from experimental water vapour sorption isotherms [30] by using *Kelvin's* law (along with the porosity and the apparent density of the dry material) [29]. A proper fitting of the capillary pressure curve is obtained through the analytical formula proposed by *van Genuchten* [50] (see Eq. (14)):

$$p_c(S_l) = a\left[S_l^{-1/m} - 1\right]^{1-m} \qquad (14)$$

where a (the so-called capillary modulus, in MPa) and m are fitting parameters dependent on the pore structure of the material.

Such a fitting has been applied here, as illustrated in Fig. 5 for mortars M1N and M2, in order to incorporate a continuous curve in the model.

3.3. Relative permeabilities

The variations of the relative permeabilities $k_{r\alpha}(s_l)$ *vs.* S_l are approached here using *Mualem's* model [45], which uses the capillary pressure curves (for adsorption and for desorption) as input data.

By defining $L = S_{la}$ and $H = (S_{ld} - S_{la}) / (1 - S_{la})$, where the a and d subscripts correspond to the main adsorption or desorption curves, respectively, the domain theory proposed by *Mualem* [45] is applied here to derive numerically $k_{rl}(s_l)$ [18,60] (see Eq. (15)):

$$k_{rl}(S_l) = S_l^{1/2}[KL + (1 - KL)KH]^2 \qquad (15)$$

where KL and KH are two normalised integral functions (see Eqs. (16) and (17)):

$$KL(S_l) = \left(\int_{p_c(S_l)}^{+\infty} dL(S_l) / p_c(S_l)^2\right) / \left(\int_0^{+\infty} dL(S_l) / p_c(S_l)^2\right) \qquad (16)$$

$$KH(S_l) = \left(\int_{p_c(S_l)}^{+\infty} dH(S_l) / p_c(S_l)^2\right) / \left(\int_0^{+\infty} dH(S_l) / p_c(S_l)^2\right) \qquad (17)$$

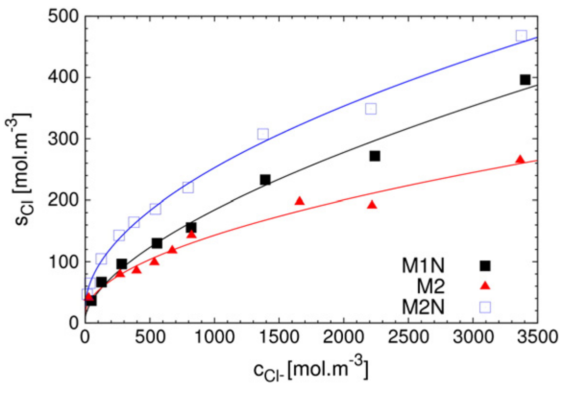

Fig. 3. Experimental chloride binding isotherms and curve fitting by means of Eq. (12) for mortars M1N, M2 and M2N at the age of 90 days.

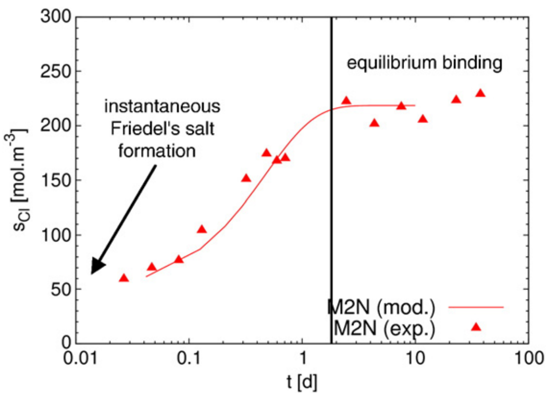

Fig. 4. Evolution of the bound chloride amount *vs.* time for mortar M2N, deduced from the decrease in the chloride concentration of the external solution $^0(c_{Cl-}$ ext. = 563 mol·m^{-3}) [4].

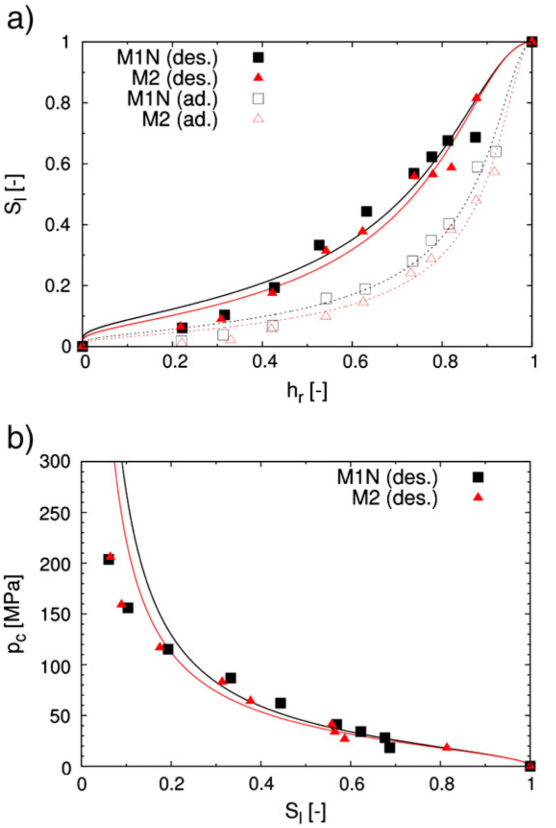

Fig. 5. Water vapour adsorption and desorption isotherms and capillary pressure curves of mortars M1N and M2 at the age of 90 days (experimental data [44] and curve fitting by means of *Kelvin's* law and Eq. (14)). a) Water vapour adsorption and desorption isotherms. b) Capillary pressure curves (desorption only).

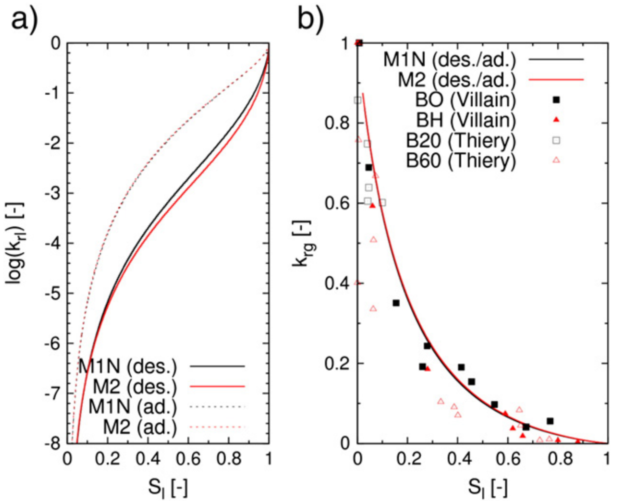

Fig. 6. Relative permeabilities to liquid and to gas *vs.* S_l (according to Eqs. (15) and (18)) for mortars M1N and M2 and experimental k_{rg} data for various concretes [18,52]. a) Relative permeability to liquid (krl). b) Relative permeability to gas (krg).

The analytical relationship $k_{rl}(S_l) = S_l^{1/2}(1-(1-S_l^{1/m})^m)^2$ derived by *van Genuchten* [50], where m is the parameter deduced from non-linear fitting of experimental $p_c = p_c(S_l)$ data (see Eq. (14)), is easier to use from a numerical point of view and is therefore often incorporated in moisture transport models. But this equation is only valid in the case of adsorption (and not of desorption) [60].

The $k_{rl} = k_{rl}(s_l)$ curves obtained for mortars M1N and M2 by using Eq. (15) with the m values given in Table 1 are reported in Fig. 6a. As expected [17,18], the same curves are obtained whatever the material. In the desorption case, Fig. 6a shows that, when $S_l < 0.40$, k_{rl} becomes very low (less than 10^{-4}). This threshold value is related to the disconnection of the liquid phase. Therefore, it will be assumed in the modelling that $k_{rl} = 0$ (*i.e.* no Darcian liquid transport) when $S_l < 0.40$.

The analytical relationship proposed by *van Genuchten* [50] (see Eq. (18)) is used here to express $k_{rg}(s_l)$:

$$k_{rg}(S_l) = (1-S_l)^p\left[1-S_l^{1/m}\right]^{2m} \qquad (18)$$

where p is a fitting parameter.

The value p = 5.5 has been proposed by *Monlouis–Bonnaire* et al. [51] for cementitious materials. However, it has been shown in Ref. [17] that this value yields some differences between analytical results and the experimental data provided in Ref. [52] within the mid saturation range, for the concretes considered. Therefore, here p has been fitted to reproduce as well as possible the experimental relative permeabilities to gas given in Refs. [18] and [52]. The best fitting thus provided p = 3.5, whatever the mix-design (see Fig. 6b) [18], pointing out an almost intrinsic behaviour for k_{rg} (given also the weak variability of parameter m). Consequently, for mortars M1N and M2, the predicted relationships $k_{rg} = k_{rg}(S_l)$ are very similar and are consistent with the experimental data obtained for various concretes (see Fig. 6b).

3.4. Intrinsic permeability

The intrinsic permeability K defined in Eq. (1) can be assessed by numerical inverse analysis. The method used here consists in comparing the relative mass loss *vs.* time plots (kinetics) of a sample submitted to a 1-D drying test (at a given RH and at constant temperature) predicted by a model (here the moisture transport model involved in the proposed coupled model) and the ones experimentally recorded, as proposed in Refs. [17,18]. In addition, this method requires the assessment of some basic material properties: the porosity and the water vapour adsorption or desorption isotherm. The water vapour diffusion coefficient involved in the equation can easily be computed thanks to Eq. (3) (see Section 2.1) and Eq. (19) (see Section 3.5). Moreover, S_l^0 has to be known. It usually corresponds to almost saturated conditions ($S_l^0 \approx 1$). K is hence deduced from the best fitting of the drying kinetics predicted by the model on the values observed for the sample submitted to the drying test. When the sorption isotherm is known and a model is available, this method has the advantage of requiring simple experiments, which do not need any specific apparatus and which can be carried out easily in every lab.

This method has been applied here to M1N and M2 samples exposed (by one side) to RH = 4% and RH = 55% after saturation ($S_l^0 \approx 1$) (see Fig. 7). In order to insure 1-D conditions, the samples were sealed by adhesive aluminium foil sheets or epoxy resin, except their drying surface. The results of the fitting process are illustrated in Fig. 7 and the K values are reported in Table 1. Whatever the boundary condition (B.C.) n(RH = 4% or RH = 55%), the K values are similar. This proves the relevance of the model to reflect the intrinsic feature of K.

3.5. Resistance factor

Numerous formulas have been proposed by researchers for the resistance factor $f(\phi, s_l)$, which is involved in *Fick's* first law (see Eq. (3)). A formula similar to that proposed by *Millington and Shearer* [49] is used here (see Eq. (19)):

$$f(\phi, S_l) = \phi^x(1-S_l)^y \qquad (19)$$

where x and y are fitting parameters.

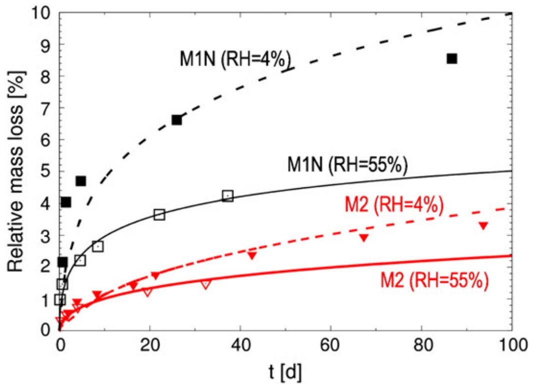

Fig. 7. Assessment of the intrinsic permeability (K) by numerical inverse analysis: fitting of drying kinetics of mortar samples exposed to RH = 4% or 55% and to T = 20 ± 1 °C [4].

Calibration with O_2 and CO_2 diffusion coefficient measurements on partially saturated mortars performed by *Papadakis* et al. [43] provides the values x = 2.74 and y = 4.20 [46]. The corresponding functions are reported in Fig. 8 and are compared to the experimental data reported in Ref. [43].

3.6. Effective ionic diffusion coefficients of partially saturated materials

The assessment of effective ionic diffusion coefficients in non-saturated conditions is difficult. As in the case of diffusion within the gas mixture, the effective diffusion coefficient for each ion is the product of the self-diffusion coefficient for the considered ion and of a resistance factor, which depends on S_l and ϕ.

The dependence on ϕ (at $S_l = 1$) is assessed from the measurement of the effective chloride diffusion coefficient in saturated conditions $D_{Cl-}(S_l = 1)$. Thus, $D_i(S_l = 1)$, with $i \neq Cl^-$, is drawn from *Nernst–Einstein* equation (see Eq. (20)) [19]:

$$\frac{D_i(S_l = 1)}{D_i^0} = \frac{D_{Cl^-}(S_l = 1)}{D_{Cl^-}^0} \qquad (\text{for } i \neq Cl^-) \qquad (20)$$

where D^o_{Cl-} and D^o_i are the diffusion coefficients in an infinitely diluted solution (self-diffusion coefficient).

The effective chloride diffusion coefficient of the saturated material $D_{Cl-}(S_l = 1)$ can be assessed experimentally (for example by steady-state or nss migration test) [19,57]. $D_{Cl-}(S_l = 1)$ can also be identified by numerical inverse analysis thanks to the proposed model. In this case, a tcc profile obtained after a nss diffusion test in lab is required [58]. Here, the tcc profiles obtained after 7-day and 48-day exposures to a 33-g·L^{-1} NaCl solution (+1 g·L^{-1} NaOH + 4.65 g·L^{-1} KOH), for mortars M1N/M2N and M2 respectively, and reported in Ref. [4], have been used to carry out the inverse analysis (see Fig. 9). The cylindrical specimens (diam. = 120 mm and thick. = 20 mm) have been saturated by an alkaline solution (1 g·L^{-1} NaOH + 4.65 g·L^{-1} KOH) before the nss diffusion test. $D_{Cl-}(S_l = 1)$ is obtained by fitting the computed tcc profile on the measured one. An algorithm has been used to minimise the difference between them [58]. The resulting values for M1N, M2 and M2N are reported in Table 1. The impact on the profiles of the kinetic effect described in Eq. (13) is depicted in Fig. 9. When this effect is considered for chloride adsorption, the chloride penetration front is located slightly beyond the front obtained in the case of equilibrium binding. Since the formation of *Friedel's* salt induces a step in the tcc profile [24], the kinetic effect softens up the foot part of the tcc profile, which is rather sharp in the case of equilibrium binding.

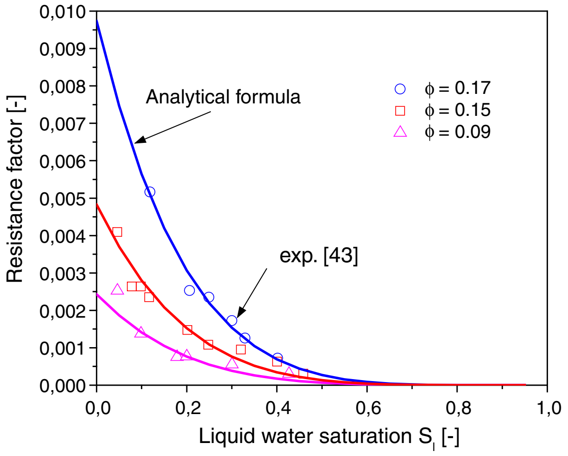

Fig. 8. Resistance factor *vs.* S_l: experimental data [43] and curve fitting by Eq. (19) [46].

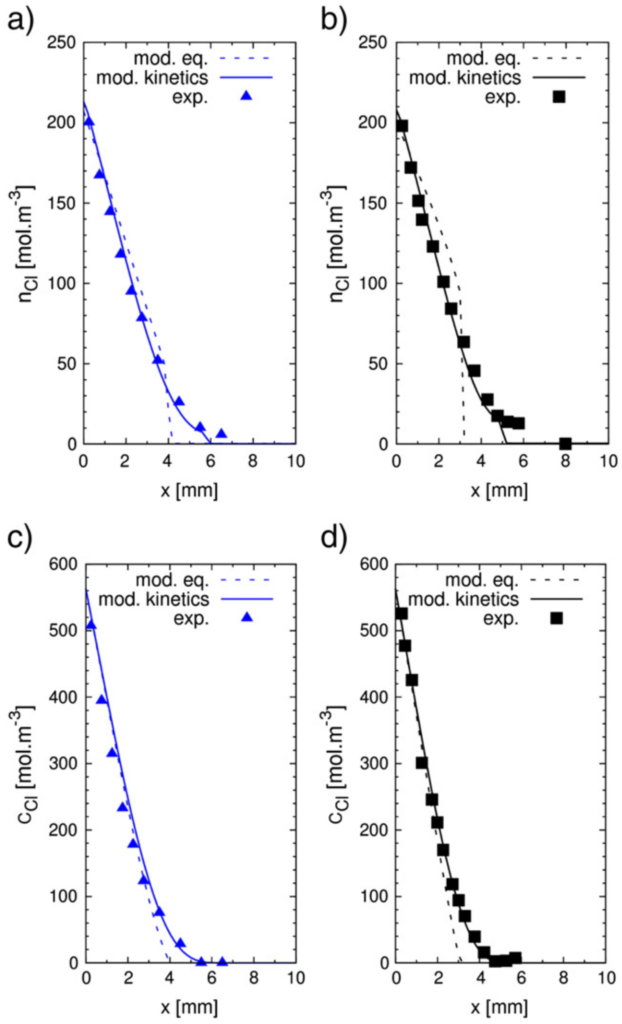

Fig. 9. Total chloride concentration (tcc) and free chloride concentration (fcc) profiles obtained experimentally after 7-day and 48-day nss diffusion tests in lab, for mortars M1N and M2 respectively [4]. Comparison with numerical simulations in the cases of equilibrium binding and delayed binding. a) M1N — tcc profile (7-day exposure). b) M2 — tcc profile (48-day exposure). c) M1N — fcc profile (7-day exposure). d) M2 — fcc profile (48-day exposure). n_{Cl} is expressed in mol/m^3 of concrete, whereas c_{Cl} is expressed in mol/m^3 of solution.

With regard to the dependence on S_l, here, the same type of semi-empirical formula as proposed by *Buchwald* in Ref. [27] for masonry materials is adopted for the relative chloride diffusion coefficient dr_{Cl-} (see Eq. (21)):

$$dr_{Cl-} = D_{Cl-}(s_l) / D_{Cl-}(s_l = 1) = s_l^{\lambda} \tag{21}$$

where λ is the saturation exponent.

Calibration of this formula with the chloride diffusion coefficient values measured by impedance spectroscopy on four mortar mixtures for various degrees of saturation and provided in Ref. [4], and assuming that the same curve is valid whatever the cementitious material, (similarly as in the case of k_{rl}), yields $\lambda = 6$ (see Fig. 10). Eq. (21) is of importance with regard to the quantification of the coupling between moisture and chloride transports. According to the fitting displayed in Fig. 10, $d_{rl} \approx 0$ when $S_l < 0.40$, as for k_{rl}. This would indicate that the liquid phase is disconnected and that ionic diffusion becomes negligible when $S_l < 0.40$. But note that no experimental data were available for $S_l < 0.70$. Therefore, it is difficult to provide a realistic fitting in this range.

3.7. Initial composition of the pore solution

The initial composition of the pore solution of a material in saturated conditions can be calculated by means of the method based on *Taylor's* work (detailed in Refs. [53,55]), which requires the mix-composition, the chemical composition of the cement and a hydration model. The computation of the alkali concentrations of the pore solution c_{Na+} and c_{K+} (in mol/m^3 of solution) in saturated conditions involves the concentrations of alkalis released from the cement $c_{Na+(released)}$ and $c_{K+(released)}$ and of alkalis adsorbed onto the hydration products $c_{Na+(adsorbed)}$ and $c_{K+(adsorbed)}$ [53] (see Eq. (22)):

$$c_{Na+} = c_{Na+(released)} - c_{Na+(adsorbed)} \left(\text{idem for } K^+\right). \tag{22}$$

The alkalis released from the cement are instantaneously released from highly soluble salts (such as Na_2SO_4) or progressively released from clinker phases during their hydration [53,55] (see Eq. (23)):

$$\begin{aligned} c_{Na+(released)} = {} & f_{Na,sulphate} c_{Na+(T)} \\ & + \left(1 - f_{Na,sulphate}\right) \alpha c_{Na+(T)} \qquad \left(\text{idem for } K^+\right) \end{aligned} \tag{23}$$

where $f_{Na,sulphate}$ is the fraction of Na^+ present in sulphate salts ($f_{Na,sulphate} = 0.35$ and $f_{K,sulphate} = 0.55$ according to Ref. [54]), while α is the degree of hydration of the cement.

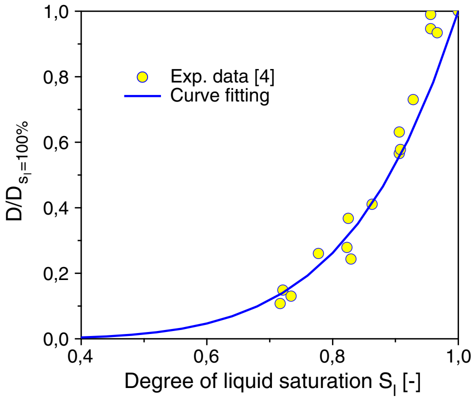

Fig. 10. Relative values of effective chloride diffusion coefficient *vs.* S_l.

The total alkali concentrations $c_{Na+(T)}$ and $c_{K+(T)}$ (in mol/m^3 of solution) can be computed from the corresponding mass fractions and molar masses (see Eq. (24)):

$$c_{Na+(T)} = 2 \frac{C\,\varphi_{Na_2O}}{\phi\, M_{Na_2O}} \left(\text{idem for } K^+\right) \tag{24}$$

where φ_{Na2O} denotes the Na_2O content of the cement (in kg·kg^{-1}), M_{Na2O} the molar mass of Na_2O (in kg·mol^{-1}) and C the cement content deduced from the mix-composition (in kg·m^{-3}).

According to Refs. [33,53,63], alkali adsorption takes place mainly onto C–S–H and the adsorbed alkali concentrations thus read (see Eq. (25)):

$$c_{Na+(adsorbed)} = c_{Na+} \cdot \frac{R_d \cdot n_{C-S-H}}{\phi} \left(\text{idem for } K^+\right) \tag{25}$$

where R_d is the distribution ratio and n_{C-S-H} is the C–S–H content of the material (here in kg/m^3 of material). R_d values of 0.39 and 0.38 m^3/kg of C–S–H are assumed for Na^+ and K^+ respectively according to Ref. [33]. For mixtures with silica fume, a R_d value of 0.7 m^3/kg of C–S–H for both Na^+ and K^+ is chosen in Ref. [55].

n_{C-S-H}, ϕ and α can be deduced from the mix-composition, the chemical composition of the cement and the hydration kinetics of the cement by using the numerical hydration model proposed in Ref. [56] (see Fig. 11a and b).

The alkali concentrations of the pore solution (in saturated conditions) of mortars M1N and M2, at the age of 90 days, obtained by the described method are displayed in Fig. 11c. In the case of M2, the alkali content of the SF has been taken into account. Note that very good agreement with experimental data was obtained when applying this method with cement pastes after a hydration period of 7 days [23]. The initial degree of saturation S_l^0 in the various test conditions, as well as the composition of the saturation solution if any, need to be considered, in order to assess the actual initial ionic concentrations of the pore solution of the various tested samples (see Section 4).

The initial chloride concentration is assumed to be equal to zero. Thus, the initial hydroxyl concentration in saturated conditions is calculated by considering the electroneutrality of the pore solution, which simplifies as follows (see Eq. (26)), since the calcium concentration in the pore solution is low when alkalis are present (pH>12.4):

$$c_{OH-} = c_{Na+} + c_{K+} \tag{26}$$

4. Application and validation of the proposed model in lab conditions

Simulations in various cases of moisture–chloride transport have been carried out with the proposed model on the 90-day water-cured mortars M1N and M2 (see Section 3). The required input data are given in Table 1. The numerical simulations have been compared to experimental data available in the literature, in order to investigate the capability of the model to predict moisture and ionic profiles.

4.1. Capillary water absorption

40 × 40 × 20 mm M1N samples have been submitted to 48-hour capillary water (+1 g·L^{-1} NaOH + 4.65 g·L^{-1} KOH) absorption after drying at RH = 4% until mass stabilisation (after this drying process $S_l^0 = 0.09$, see Fig. 5a) [4]. The samples were laterally sealed, in order to insure 1-D transport processes. The moisture profiles after various exposure times have been simulated by using the ϕ value reported in Table 1 and the K value obtained from fitting of drying data at RH = 4% (see Table 1 and Fig. 7). The water vapour adsorption isotherm (see

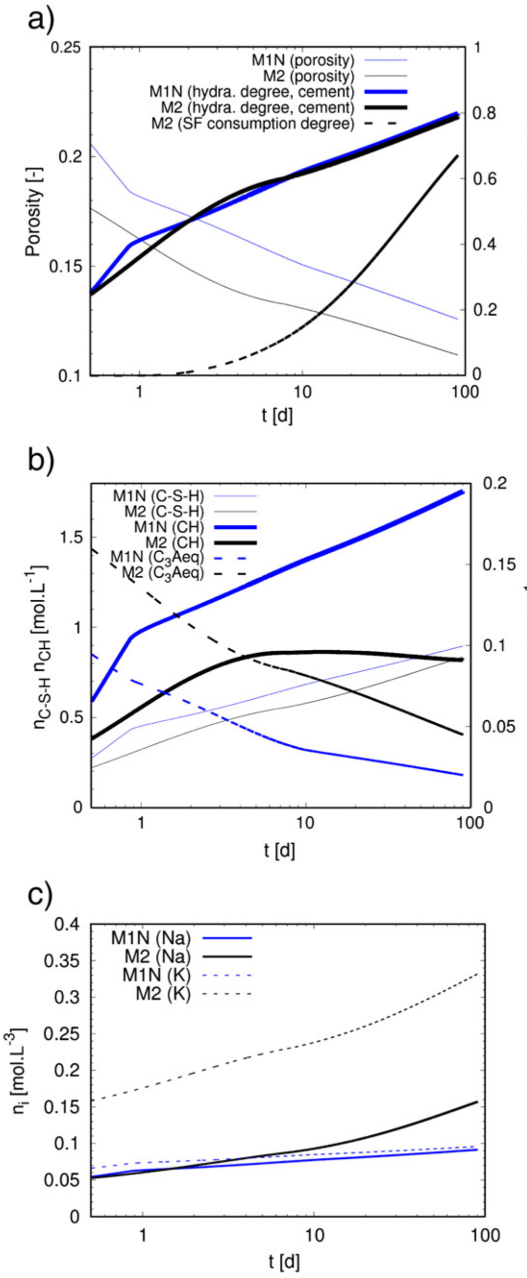

Fig. 11. Assessment of porosity, degrees of reaction of the cement and of the silica fume, n_{C-S-H}, n_{CH} and $n_{(C3A)eq.}$, and alkali concentrations of the pore solution, for mortars M1N and M2 (in saturated conditions) at the age of 90 days. a) ϕ and degrees of reaction of cement and SF, computed by the numerical hydration model described in Ref. [56]. b) n_{C-S-H}, n_{CH} and $n_{(C3A)eq.}$ computed by the numerical hydration model described in Ref. [56]. c) Alkali concentrations of the pore solution assessed by the described method (in saturated conditions).

Table 1 and Fig. 5a), along with the $k_{rl}=k_{rl}(S_l)$ analytical formula, has been used.

The numerical moisture profiles are compared in Fig. 12 to the gamma-ray attenuation measurements reported in Ref. [4] after various exposure times. Rather good agreement is observed between numerical and experimental profiles. Hence, the intrinsic permeability obtained from a drying test can be used to describe the liquid water absorption process, provided that appropriate capillary pressure curve and relative permeability formula (*i.e.* for adsorption) are chosen. In Fig. 12, the rapid progress of the wetting front is clearly visible. As pointed out by both numerical and experimental results, after 48-hour exposure, the degree of saturation is very high within the sample. Note that since not many experimental plots are available, it is difficult to deduce the actual experimental trend and therefore to propose interpretations for the small difference recorded between numerical and experimental profiles.

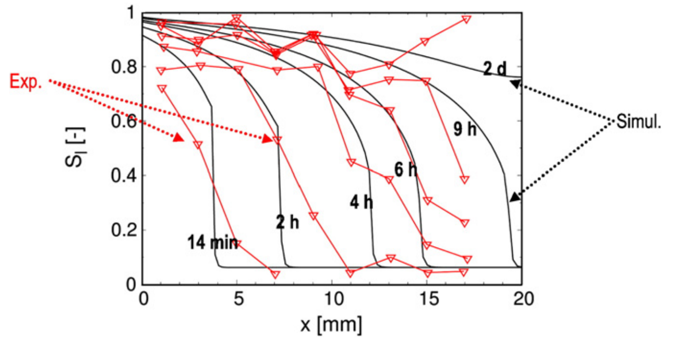

Fig. 12. Moisture profiles after various exposure times to capillary water absorption for a M1N sample (initial condition: $S_l^0=0.09$). Comparison between numerical simulations and gamma-ray attenuation measurements [4].

4.2. Wetting by a NaCl solution after drying

The wetting experiments reported by *Francy* in Ref. [4] are considered here. Cylindrical samples (diam. = 120 mm and thick. = 20 mm) of mortars M1N and M2 have been exposed for 48 h to a 33-$g \cdot L^{-1}$ NaCl solution (+ 1 $g \cdot L^{-1}$ NaOH + 4.65 $g \cdot L^{-1}$ KOH) after drying at RH = 4% (after this drying process $S_l^0=0.09$ for M1N and M2, see Fig. 5a). The B.Cs. are: $c_{Cl-}=563$, $c_{OH-}=108$, $c_{Na+}=588$ and $c_{K+}=83$ $mol \cdot m^{-3}$ (pH = 13.0). The initial composition of the pore solution is assumed here to be imposed by the solution used for saturation (1 $g \cdot L^{-1}$ NaOH + 4.65 $g \cdot L^{-1}$ KOH), initial alkali binding [63] and S_l^0: $c^0_{Cl-}=0$, $c^0_{OH-}=722$, $c^0_{Na+}=144$ and $c^0_{K+}=578$ $mol \cdot m^{-3}$ (pH = 13.8) for M1N and M2. The samples were sealed (except the exposed surface at x = 0), in order to insure 1-D transport. Therefore, the B.C. at x = 20 mm is a non-exchange condition. The ϕ, $D_{Cl-}(S_l=1)$ and K values given in Table 1 have been used. The water vapour adsorption isotherm (see Table 1 and Fig. 5a), along with the $k_{rl}=k_{rl}(S_l)$ analytical formula, has been used.

The numerical moisture profiles at various exposure times are reported in Fig. 13. The tcc profiles after various exposure times have also been simulated (see Fig. 14) and the tcc profile obtained after 24 h has been compared to the experimental data obtained by grinding of the samples and chemical analysis (by potentiometric titration of the powder specimens then obtained [4]) (see Fig. 14).

After 24-hour exposure, the wetting front has reached the boundary of the M1N sample: $S_l=1$ throughout the sample (see Fig. 13). The better efficiency of M2 (mainly as a result of incorporation of SF in the mixture) to limit moisture transport is obvious in Fig. 13.

As depicted in Fig. 14, after 24-hour exposure, when equilibrium chloride binding is considered, the model largely overestimates the tcc in the near surface zone and significantly underestimates the chloride penetration depth. This last effect is clearly prejudicial from the structural safety point of view. When chloride binding is disregarded in the model, simulations are significantly more satisfactory, at least with regard to the chloride penetration front zone (see Fig. 14). As a matter of fact, the chloride penetration depth is significantly closer to the experimental value and is slightly higher. This is therefore a more conservative approach. However, the best agreement with experimental data (after 24-hour exposure) is obtained when a delay effect is included in the binding description (see Section 3.1). The binding kinetics was not available for the

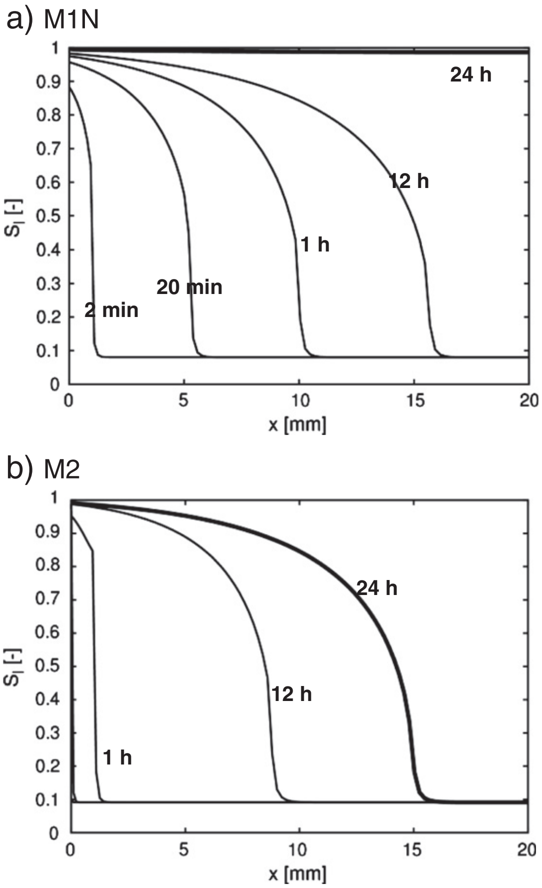

Fig. 13. Numerical moisture profiles of mortar samples exposed to a salt solution ($33\ g \cdot L^{-1}$ NaCl + $1\ g \cdot L^{-1}$ NaOH + $4.65\ g \cdot L^{-1}$ KOH) after drying (various exposure times and initial condition: $S_l^0 = 0.09$). Exposed surface on the left.

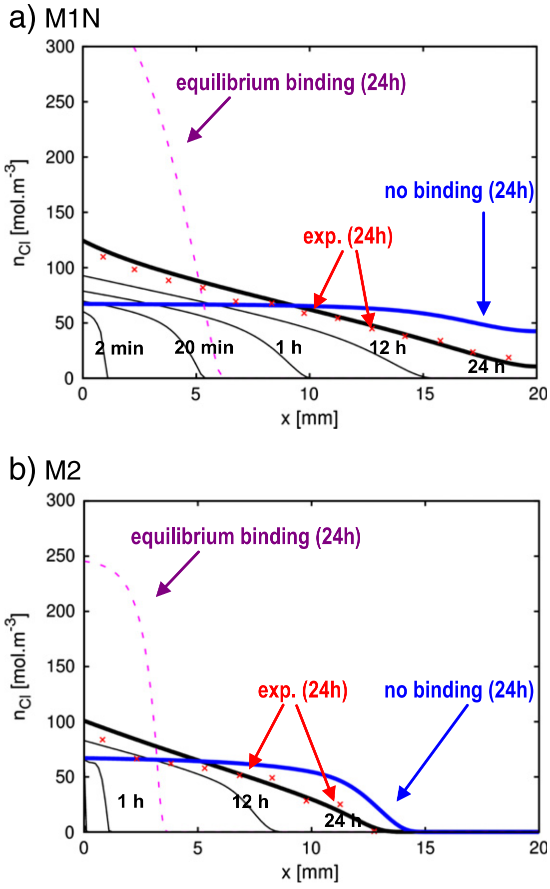

Fig. 14. Numerical tcc profiles of mortar samples exposed to a salt solution ($33\ g \cdot L^{-1}$ NaCl + $1\ g \cdot L^{-1}$ NaOH + $4.65\ g \cdot L^{-1}$ KOH) after drying (various exposure times and initial condition: $S_l^0 = 0.09$). Comparison between numerical and experimental [4] tcc profiles after 24-hour exposure. Exposed surface on the left.

materials tested here. Therefore, the characteristic time τ has been obtained by fitting the simulated tcc at the exposed surface on the extrapolated one (from the measured profile), since the chloride concentration is imposed at the exposed surface as in the case of Fig. 4. $\tau \approx 10$ h (3.6×10^4 s) has been found for both mortars, thus indicating an intrinsic feature. Moreover, this value is close to the characteristic time (2×10^4 s) obtained with another mortar (M2N, see Section 3.1) from its binding kinetics (see Fig. 4). All of this emphasises the importance of accounting in models for the appropriate chloride binding description in saturated and also in non-saturated conditions. The better efficiency of M2 to limit chloride ingress is clearly visible in Fig. 14.

The ionic concentration profiles predicted after 12-hour and 24-hour exposure ($S_l^0 = 0.09$) are compared to the profiles predicted in the case where the initial condition is $S_l^0 = 1$ in Figs. 15 and 16, for M1N and M2 respectively. In the case $S_l^0 = 1$, the test takes place in saturated conditions, therefore the model can be simplified into the multispecies transport model (where only ionic diffusion, along with chemical activity effects and electrical interactions, is considered). The initial composition of the pore solution is assumed to be in this case (as a result of the composition of the saturation solution and initial alkali binding [63]): $c^0_{Cl-} = 0$, $c^0_{OH-} = 65$, $c^0_{Na+} = 13$ and $c^0_{K+} = 52\ mol \cdot m^{-3}$ for M1N and M2. As illustrated in Figs. 15 and 16, when advection takes place in addition to diffusion ($S_l^0 = 0.09$), a faster Cl^- (and Na^+) ingress is observed and a higher c_{Cl-} is obtained at a given depth, since these ions move along with the liquid phase. In saturated conditions (diffusion case, see Figs. 15b and 16b), a faster Na^+ ingress is observed, compared to Cl^- ingress, since no binding is assumed in the case of Na^+ transport, whereas equilibrium binding is considered in the case of Cl^- transport. When $S_l^0 = 0.09$, Cl^- and Na^+ penetration fronts are very close (see Figs. 15a and 16a). This indicates that for these ions the advective transport is predominant. It can also be noted that the Cl^- penetration front and the wetting front do not coincide exactly. This results from the dilution of the "external" solution into the solution initially present in the pore system. This dilution effect also induces a decrease in c_{Na+}, c_{OH-} and c_{K+} at the wetting front. As expected, c_{OH-} decreases within the near surface zone as a result of its lower concentration in the external solution (see Figs. 15 and 16). The peak recorded for c_{OH-} in the case $S_l^0 = 1$ (see Figs. 15b and 16b) results from OH^- release, in order to (electrically) balance equilibrium Cl^- binding. The significant difference recorded between the results provided in the cases $S_l^0 = 1$ and $S_l^0 = 0.09$ points out that the low initial S_l value has induced a tcc profile, which cannot be predicted by a model developed in saturated conditions. This emphasises the major contribution of advection to the overall ionic transport and thus the importance of liquid permeability in the model, and therefore in the prediction of chloride ingress in non-saturated conditions.

4.3. Wick action test

Wick action is the transport of liquid trough a cementitious element from a surface in contact with a solution towards a drying surface [41,42]. The wick action test described by *Francy* in Ref. [4] on a 25-mm thick cylindrical M1N sample has been simulated by the model described in this paper. In this test, the initially saturated

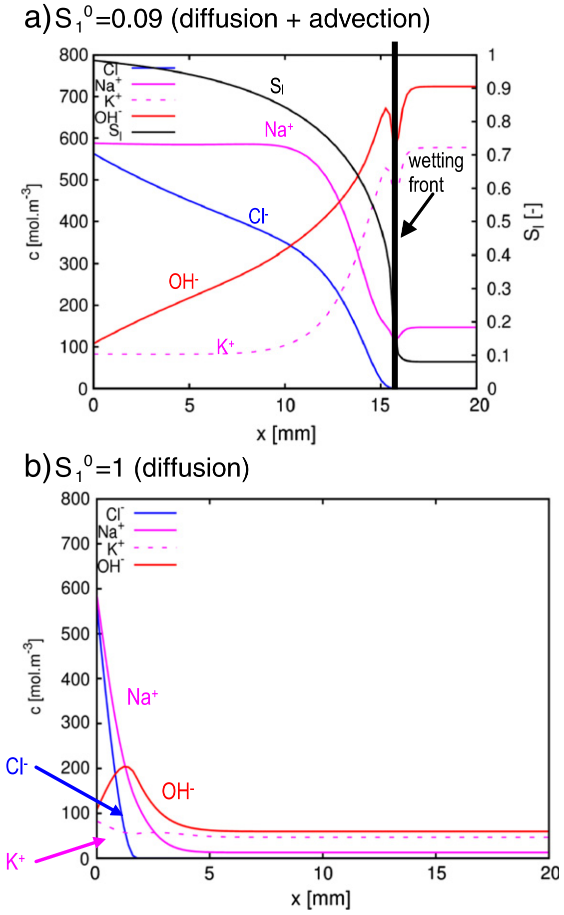

Fig. 15. Ionic concentration and moisture profiles predicted in M1N after 12-hour exposure to a salt solution ($33\ g\cdot L^{-1}$ NaCl + $1\ g\cdot L^{-1}$ NaOH + $4.65\ g\cdot L^{-1}$ KOH). Exposed surface on the left.

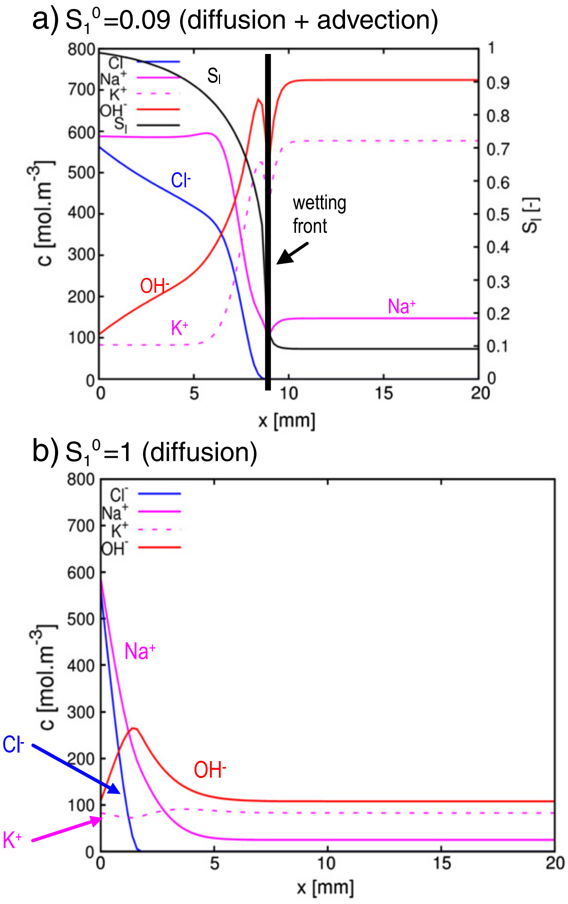

Fig. 16. Ionic concentration and moisture profiles predicted in M2 after 24-hour exposure to a salt solution ($33\ g\cdot L^{-1}$ NaCl + $1\ g\cdot L^{-1}$ NaOH + $4.65\ g\cdot L^{-1}$ KOH). Exposed surface on the left.

sample is exposed to a $33\text{-}g\cdot L^{-1}$ NaCl solution ($+1\ g\cdot L^{-1}$ NaOH + $4.65\ g\cdot L^{-1}$ KOH) at one of the plane surfaces (upstream surface at depth $x = 0$) and to RH = 9% (controlled by a KOH saturated salt solution) at the other plane surface (downstream surface at depth $x = 0.25$). The initial composition of the pore solution is assumed to be (see Section 4.2): $c^0_{Cl-} = 0$, $c^0_{OH-} = 65$, $c^0_{Na+} = 13$ and $c^0_{K+} = 52\ mol/m^{-3}$. The ϕ, $D_{Cl-}(S_l = 1)$ and K values given in Table 1 are used. Here, both the water vapour desorption and adsorption isotherms have been used (see Table 1 and Fig. 5a), along with $k_{rl} = k_{rl}(S_l)$ expressed as Eq. (15). The drying process can be separated in two stages [59]: the first one, which is particularly significant when the material is initially saturated, is controlled by the evaporation rate at the drying surface, and the second one is the moisture transport towards the drying surface. Hence, two different types of B.C. have been used here for moisture: S_l is imposed at $x = 0$ (*Dirichlet* B.C.), while moisture flux is imposed at $x = 0.25$ (*Neumann* B.C., see Eq. (27), where the wind velocity is assumed to be equal to zero). This flux is proportional to the difference between the water vapour pressure in the environment ($p_{v\ ext.}$) and the water vapour pressure in the pore network within the surface zone (p_v) (see Eq. (27)):

$$\text{at } x = 0.25 : w_w + w_v = E\phi S_l(p_v - p_{v\ ext.}) \tag{27}$$

where E is the moisture emissivity coefficient ($= 2\times10^{-8}\ kg\cdot m^{-2}\cdot s^{-1}\cdot Pa^{-1}$).

Neumann B.C. is particularly relevant when the material is initially saturated, contrary to *Dirichlet* B.C., which imposes instantaneously the S_l value beneath the environment–sample interface.

The numerical moisture and tcc profiles obtained after various exposure times are presented in Fig. 17. The ionic concentration profiles after 35-day and 4-month exposures are reported in Fig. 18.

The very low RH imposed at the downstream surface (which yields $S_l = 0.15$) induces a strong drying. This induces the formation of a zone characterised by a degree of saturation below the disconnection threshold of the liquid phase ($S_l < 0.40$) from this downstream surface (see Fig. 17a), where no Darcian liquid transport is possible (see Section 3.3), and thus of an evaporation front (characterised by $S_l = 0.40$). The thickness of this zone is increasing as a function of time until moisture flow reaches the steady-state regime, which is observed here from around 2 months (see Fig. 17a). Note that since chloride concentration is increasing at the same time, the relationship between RH and S_l changes with time (see Section 2.3).

Chlorides penetrate in the sample as a result of concentration gradients. Then, chlorides are transported by diffusion and advection towards the downstream surface. The strong drying at the downstream surface induces a significant liquid flow. Chloride transport by advection becomes rapidly prominent and induces a continuous and significant ingress of chlorides towards the downstream surface. This points out again the importance of the liquid permeability in the model. Chlorides from the upstream surface move inwards as long as S_l is high enough. Once the chloride penetration front reaches the evaporation front, chlorides accumulate at this evaporation front. Figs. 17b and 18b show that, after 4 months, chlorides have already reached the evaporation front, whereas after 35 days the chloride penetration front is still far from the evaporation front (see Fig. 18a). Ionic concentrations are very high in the vicinity of the evaporation front, owing to the very low S_l in this zone. The tcc increases as a

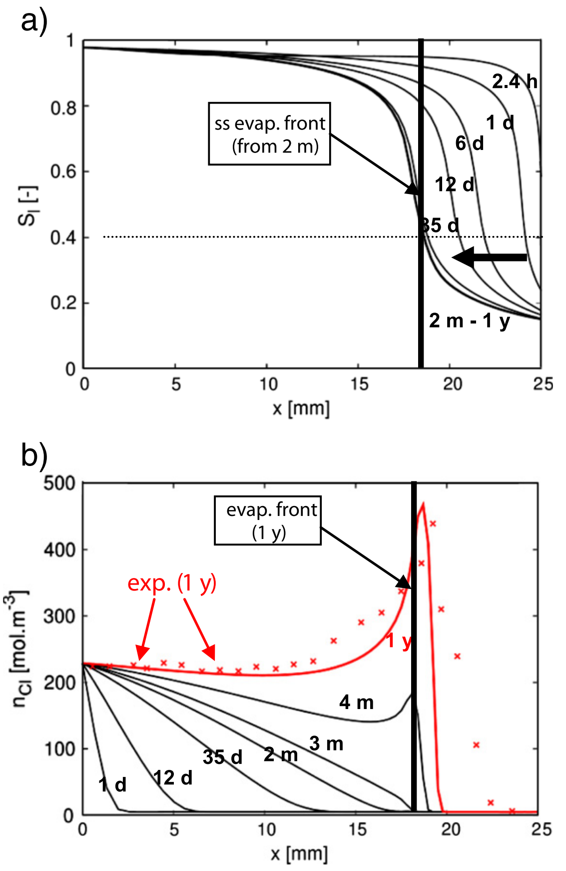

Fig. 17. Numerical moisture and tcc profiles of M1N samples during wick action test. a) Numerical moisture profiles. b) Numerical tcc profiles. Comparison with experimental data after 1 year [4].

function of time just beneath the evaporation front, as a result of the continuous chloride supply from the upstream surface. From a given time, the tcc in this zone is higher than the tcc at the upstream surface. All of this, and thus the complexity of the wick test, explains the peculiar shape of the ionic and tcc profiles. Good agreement is obtained between numerical simulations and the experimental data, which are available at 1 year. Not only the location of the evaporation front but also the tcc distribution within the whole thickness of the specimen, in particular in the vicinity of the evaporation front, are correctly predicted. Only when chloride diffusion takes place in a zone where the degree of saturation is very low ($0.15<S_l<0.40$), differences are recorded between numerical and experimental results (see Fig. 17b). This may be explained by the selection of a too small diffusion coefficient in this zone: $D_{Cl-}=D_{Cl-}(S_l)$ was deduced from fitting on experimental data obtained on mortars including M1N, but no experimental data were actually available within the range $0.15<S_l<0.40$ (see Section 3.6 and Fig. 10). Note that the delay effect, which affects chloride physical adsorption (see Section 3.1), is also taken into account in these simulations. However, contrary to the case addressed in Section 4.2, its impact here is very weak, since the wick action test is much longer (1 year) than the 24-hour wetting test and the characteristic time ($\tau \approx 10$ h).

With the mortar tested here, the evaporation front is rather close to the drying (downstream) surface. However, the location of the evaporation front, as well as the impact on the tcc profile of the drying process that takes place at the downstream surface, depends on the material and on the experimental conditions (see other experimental examples in Ref. [4]).

a) after 35 days

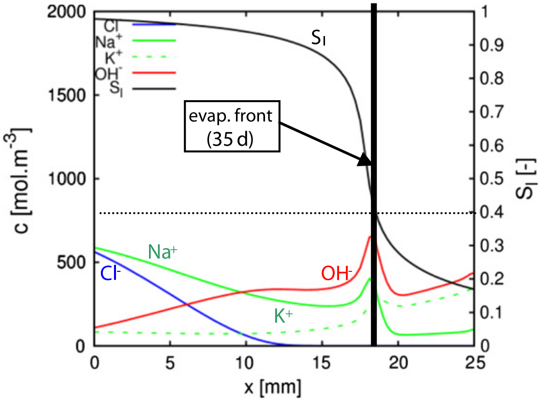

b) after 4 months

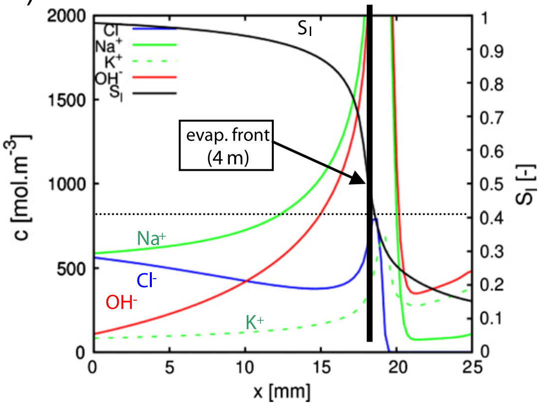

Fig. 18. Numerical ionic concentration and moisture profiles of M1N samples during wick action test.

5. Conclusion

A 1-D numerical physical model of isothermal coupled moisture–ion transport in cementitious materials has been presented in this paper. In its current state, this model includes the following phenomena: diffusion, advection, electrical interactions between ions, ion effect on liquid/vapour water equilibrium, instantaneous and delayed chloride binding. The model requires as input data key material properties, which have well-identified physical meaning. These material properties can accurately be assessed by the methods described in the paper, in particular by numerical inverse analysis. As illustrated by the examples displayed in this paper, the model has been validated on mortars in lab conditions (first stage of validation) in various configurations (*e.g.* wetting by a salt solution after drying or wick action test). These examples have emphasised the reliability and the efficiency of the proposed model to predict moisture, ionic concentrations and tcc profiles. The model is capable of predicting all the complex effects associated with coupled moisture–ion transport on the profiles (in particular in the vicinity of the evaporation front in the case of the wick action test). In addition, the model developed and the examples presented in this paper contribute to a better understanding of the mechanisms, which govern such a coupled transport in cementitious materials. In particular, it has been pointed out that binding cannot be assumed as instantaneous when the chloride velocity is high (case of high-rate advective transport in the short term) and a kinetic effect has to be considered to account for the experimental behaviour. In addition, the major contribution of advection to the overall ionic transport and thus the importance of liquid permeability in the model and therefore in the prediction of chloride ingress in non-saturated conditions, has been highlighted. Only a model that combines liquid-water and water-vapour transport processes with aqueous electrolyte theory will allow long-term accurate predictions for every types of natural environment (*e.g.* tidal zone or spraying of deicing salts) and material. Validation of the proposed model in field conditions (second stage) remains to be done. The proposed model will then be part of a simulation tool of more general applicability for partially saturated concrete.

References

[1] T.J. Kirkpatrick, R.E. Weyers, M.M. Sprinkel, C.M. Anderson-Cook, Impact of specification changes on chloride-induced corrosion service life of bridge decks, Cem. Conc. Res. 32 (8) (2002) 1189–1197.

[2] V. Baroghel-Bouny et al., Concrete design for a given structure service life — Durability management with regards to reinforcement corrosion and alkali-silica reaction. State-of-the-art and guide for the implementation of a predictive performance approach based upon durability indicators, Scientific and Technical Documents of AFGC (AFGC, Paris, issue in French: 2004 & issue in English: 2007), 240 pp.

[3] S.R. Yeomans, Performance of black, galvanized, and epoxy-coated reinforcing steels in chloride-contaminated concrete, Corrosion 50 (1) (1994) 72–81.

[4] O. Francy, Modelling of chloride ions ingress in partially water saturated mortars (in French), Ph.D. Thesis, Paul Sabatier Univ., Toulouse, France, 1998, 171 pp.

[5] T.Q. Nguyen, Physicochemical modelling of chloride ions ingress in cementitious materials (in French), Ph.D. Thesis, ENPC, Marne-la-Vallée, France, 2007, 233 pp.

[6] I.N. Nassar, R. Horton, A.M. Globus, Simultaneous transfer of heat, water, and solute in porous media: II. experiment and analysis, Soil Sci. Soc. Am. J. 56 (1992) 1357–1365.

[7] V. Baroghel-Bouny, T. Chaussadent, A. Raharinaivo, Experimental investigations on binding of chloride and combined effects of moisture and chloride in cementitious materials, in: L.O. Nilsson, J.P. Ollivier (Eds.), Proc. 1st Int. RILEM Workshop “Chloride Penetration into Concrete”, Oct. 15–18, 1995, Saint-Rémy-lès-Chevreuse, France, Pro, 2, RILEM, Paris, 1997, pp. 290–301.

[8] D. Benavente, M.A. Garcia del Cura, S. Ordornez, Salt influence on evaporation from porous building rocks, Constr. Build. Mater. 17 (2003) 113–122.

[9] J.J. Beaudoin, V.S. Ramachandran, R.F. Feldman, Interaction of chloride and C–S–H, Cem. Conc. Res. 20 (1990) 875–883.

[10] A.K. Suryavanshi, J.D. Scantlebury, S.B. Lyon, Mechanism of Friedel's salt formation in cements rich in tri-calcium aluminate, Cem. Conc. Res. 26 (1996) 717–727.

[11] U.A. Birnin-Yauri, F.P. Glasser, Friedel's salt, $Ca_2Al(OH)_6(Cl,OH).2H_2O$: its solid solutions and their role in chloride binding, Cem. Conc. Res. 28 (1998) 1713–1723.

[12] A.V. Saetta, R.V. Scotta, R.V. Vitaliani, Analysis of chloride diffusion into partially saturated concrete, ACI Mater. J. 90 (5) (1993) 441–451.

[13] A. Neville, Chloride attack of reinforced concrete: an overview, Mater. Struct. 28 (176) (1995) 63–70.

[14] B.F. Johannesson, A theoretical model describing diffusion of a mixture of different types of ions in pore solution of concrete coupled to moisture transport, Cem. Conc. Res. 33 (2003) 481–488.

[15] S.J.H. Meijers, J.M.J.M. Bijen, R. de Borst, A.L.A. Fraaij, Computational results of a model for chloride ingress in concrete including convection, drying–wetting cycles and carbonation, Mater. Struct. 38 (2005) 145–154.

[16] L.O. Nilsson, WP4 report — modelling of chloride ingress, CHLORTEST – EU Funded Research Project “Resistance of Concrete to Chloride Ingress – From Laboratory Tests to In-Field Performance” G6RD-CT-2002-0085, Deliverables D14-15, 2005, 112 pp.

[17] V. Baroghel-Bouny, Water vapour sorption experiments on hardened cementitious materials. Part II: essential tool for assessment of transport properties and for durability prediction, Cem. Conc. Res. 37 (3) (2007) 438–454.

[18] M. Thiery, V. Baroghel-Bouny, N. Bourneton, G. Villain, C. Stefani, Modelling of drying of concrete — analysis of the different moisture transport modes (in French), Rev. Euro. Gén. Civ. 11 (5) (2007) 541–577.

[19] O. Truc, J.P. Ollivier, L.O. Nilsson, Multi-species transport in saturated cement-based materials, in: C. Andrade, J. Kropp (Eds.), Proc. 2nd Int. RILEM Workshop “Testing and Modelling Chloride Ingress into Concrete”, Sept. 11–12, 2000, Paris, France, Pro, 19, RILEM, Paris, 2000, pp. 247–259.

[20] M. Masi, D. Colella, G. Radaelli, L. Bertolini, Simulation of chloride penetration in cement-based materials, Cem. Conc. Res. 27 (10) (1997) 1591–1601.

[21] E. Samson, J. Marchand, Numerical solution of the extended Nernst–Planck model, J. Colloid Interface Sci. 215 (1999) 1–8.

[22] L. Tang, Concentration dependence of diffusion and migration of chloride ions. Part 2: experimental evaluations, Cem. Conc. Res. 29 (1999) 1469–1474.

[23] T.Q. Nguyen, V. Baroghel-Bouny, P. Dangla, Prediction of chloride ingress into saturated concrete on the basis of a multi-species model by numerical calculations, Comp. Conc. 3 (6) (2006) 401–422.

[24] V. Baroghel-Bouny, T.Q. Nguyen, P. Dangla, Assessment and prediction of RC structure service life by means of durability indicators and physical/chemical models, Cem. Conc. Comp. 31 (8) (2009) 522–534.

[25] B. Johannesson, K. Yamada, L.O. Nilsson, Y. Hosokawa, Multi-species ionic diffusion in concrete with account to interaction between ions in the pore solution and the cement hydrates, Mater. Struct. 40 (7) (2007) 651–665.

[26] D. Conciatori, F. Laferriere, E. Brühwiler, Comprehensive modeling of chloride ion and water ingress into concrete considering thermal and carbonation state for real climate, Cem. Conc. Res. 40 (2010) 109–118.

[27] A. Buchwald, Determination of the ion diffusion coefficient in moisture and salt loaded masonry materials by impedance spectroscopy, Proc. 3rd Int. Ph.D. Symp., Vienna, Austria, vol. 2, Oct. 11–13, 2000, pp. 475–482.

[28] C.L. Lin, L.S. Lee, A two-ionic-parameter approach for ion activity coefficients of aqueous electrolyte solutions, Fluid Phase Equilibria 205 (2003) 69–88.

[29] T.Q. Nguyen, V. Baroghel-Bouny, P. Dangla, A physical model for estimating the coupled transport of moisture and chlorides in concrete, in: F. Toutlemonde, K. Sakai, O.E. Gjørv, N. Banthia (Eds.), Proc. 5th Int. Conf. on Concrete under Severe Conditions: Environment and Loading (CONSEC'07), June 4–6, 2007, Tours, France, vol. 1, LCPC, Paris, 2007, pp. 331–342.

[30] V. Baroghel-Bouny, Water vapour sorption experiments on hardened cementitious materials. Part I: essential tool for analysis of hygral behaviour and its relation to pore structure, Cem. Conc. Res. 37 (3) (2007) 414–437.

[31] V. Baroghel-Bouny, T.Q. Nguyen, P. Dangla, P. Belin, Assessment of chloride binding isotherms, in: E. Schlangen, G. de Schutter (Eds.), Proc. Int. Symp. on Concrete Modelling (CONMOD'08), May 26–28, 2008, Delft, The Netherlands, Pro, 58, RILEM Publ, Bagneux, 2008, pp. 733–743.

[32] L. Tang, L.O. Nilsson, Chloride binding capacity and binding isotherms of OPC pastes and mortars, Cem. Conc. Res. 23 (1993) 247–253.

[33] S.Y. Hong, F.P. Glasser, Alkali binding in cement paste: Part I. the C–S–H phase, Cem. Conc. Res. 29 (1999) 1893–1903.

[34] J. Letey, W.D. Kemper, L. Noonan, The effect of osmotic pressure gradients on water movement in unsaturated soil, Soil Sci. Soc. Am. Proc. 33 (1969) 15–18.

[35] D.R. Scotter, Salt and water movement in relatively dry soil, Aust. J. Soil Res. 12 (1974) 27–35.

[36] L.O. Nilsson, A model for convection of chloride, in: V. Frederiksen (Ed.), “A System for Estimation of Chloride Ingress into Concrete. Theoretical Background”, HETEK Rep. No 83, Chap. 7, The Danish Road Directorate, Copenhagen, 1997, pp. 47–68.

[37] S. Swaddiwudhipong, S.F. Wong, T.H. Wee, S.L. Lee, Chloride ingress in partially and fully saturated concretes, Conc. Sci. Eng. 2 (2000) 17–31.

[38] C. Andrade, Calculation of chloride diffusion coefficients in concrete from ionic migration measurements, Cem. Conc. Res. 23 (3) (1993) 724–742.

[39] T. Ishida, P. O'Neill Iqbal, H.T.L. Anh, Modeling of chloride diffusivity coupled with non-linear binding capacity in sound and cracked concrete, Cem. Conc. Res. 39 (2009) 913–923.

[40] R. Eymard, T. Gallouet, R. Herbin, The finite volume method, in: P. Ciarlet, J.L. Lions (Eds.), Handbook of Numerical Analysis, 2000.

[41] N.D. Buenfeld, M.T. Shurafa-Daoudi, I.M. McLoughlin, Chloride transport due to wick action in concrete, in: L.O. Nilsson, J.P. Ollivier (Eds.), Proc. 1st Int. RILEM Workshop “Chloride Penetration into Concrete”, Oct. 15–18, 1995, Saint-Rémy-lès-Chevreuse, France, Pro, 2, RILEM, Paris, 1997, pp. 315–324.

[42] J.M. Aldred, B.V. Rangan, N.D. Buenfeld, Effect of initial moisture content on wick action through concrete, Cem. Conc. Res. 34 (6) (2004) 907–912.

[43] V.G. Papadakis, C.G. Vayenas, M.N. Fardis, Physical and chemical characteristics affecting the durability of concrete, ACI Mater. J. 88 (1991) 186–196.

[44] S. Bonnet, Influence of chloride on equilibrium behaviour and on transfer properties of civil engineering materials (in French), Ph.D. Thesis, INSA, Toulouse, France, Déc. 1997, 252 pp.

[45] Y. Mualem, A new model for predicting the hydraulic conductivity of unsaturated porous media, Water Resour. Res. 12 (1976) 513–522.

[46] M. Thiery, P. Dangla, G. Villain, G. Platret, E. Massieu, M. Druon, V. Baroghel-Bouny, Modelling of atmospheric carbonation of cementitious materials, Bul. Lab. Ponts Chaus. 252–253 (2005) 153–187.

[47] E. Samson, J. Marchand, K.A. Snyder, J.J. Beaudoin, Modeling ion and fluid transport in unsaturated cement systems in isothermal conditions, Cem. Conc. Res. 35 (2005) 141–153.

[48] E. Samson, J. Marchand, Modeling the effect of temperature on ionic transport in cementitious materials, Cem. Conc. Res. 37 (2007) 455–468.

[49] R.J. Millington, R.C. Shearer, Diffusion in aggregated porous media, Soil Sci. 3 (1970) 372–378.

[50] M.Th. Van Genuchten, A closed-form equation for predicting the hydraulic conductivity of unsaturated soil, Soil Sci. Soc. Am. 44 (1980) 892–898.

[51] J.P. Monlouis-Bonnaire, J. Verdier, B. Perrin, Prediction of the relative permeability to gas flow of cement-based materials, Cem. Conc. Res. 34 (2004) 737–744.

[52] G. Villain, V. Baroghel-Bouny, C. Kounkou, C. Hua, Gas permeability measurement as a function of the saturation rate of concretes (in French), Rev. Franç. Gén. Civ. 5 (2–3) (2001) 251–268.

[53] H.F.W. Taylor, A method for predicting alkali ion concentration in cement pore solution, Adv. Cem. Res. 1 (1987) 5–16.

[54] H.W.W. Pollitt, A.W. Brown, 5th ISCC, Cement Association of Japan, Tokyo, vol. 1, 1969, p. 322.

[55] H.J.H. Brouwers, R.J. van Eijk, Alkali concentration of pore solution in hydrating OPC, Cem. Conc. Res. 33 (2) (2003) 191–196.

[56] M.D. Nguyen, Modelling coupling between hydration and desiccation of cementitious materials after removal of formworks. Study of the degradation of transfer properties (in French), Ph.D. Thesis, ENPC, Marne-la-Vallée, France, 2009, 237 pp.

[57] V. Baroghel-Bouny, K. Kinomura, M. Thiery, S. Moscardelli, Easy assessment of durability indicators for service life prediction on quality control of concretes with high volumes of supplementary cementing materials, Accepted for publication in Cem. Conc. Comp.

[58] V. Baroghel-Bouny, X. Wang, M. Thiery, Prediction of chloride binding isotherms by analytical model or numerical inverse analysis, Proc. 2nd Int. Symp. on Service Life Design for Infrastructures, Delft, The Netherlands, Oct. 4–6, 2010.

[59] M. Azenha, K. Maekawa, T. Ishida, R. Faria, Drying induced moisture losses from mortar to the environment. Part II: numerical implementation, Mater. Struct. 40 (2007) 813–825.

[60] M. Thiery, P. Belin, V. Baroghel-Bouny, M.D. Nguyen, Modelling of isothermal drying process in cementitious materials: analysis of the moisture transfer and

proposal of simplified approaches, in: J.F. Shao, N. Burlion (Eds.), Proc. 3rd Int. Conf. on Coupled THMC Processes in Geo-systems: Fundamentals, Modeling, Experiments and Applications "GeoProc 2008", June 2–6, 2008, Lille, France, 2008, pp. 571–579.

[61] D. Archer, R. Carter, Thermodynamic properties of the NaCl + H_2O system, J. Phys. Chem. 104 (2000) 8563–8584.

[62] K.S. Pitzer, Thermodynamics of electrolytes. I. Theoretical basis and general equations, J. Phys. Chem. 77 (2) (1973) 268–559.

[63] W. Chen, H.J.H. Brouwers, Alkali binding in hydrated Portland cement paste, Cem. Conc. Res. 40 (2010) 716–722.

[64] O. Bernard, F.-J. Ulm, E. Lemarchand, A multiscale micromechanics-hydration model for the early-age elastic properties of cement-based materials, Cem. Conc. Res. 33 (9) (2003) 1293–1309.

[65] E.M. Theissing, T. Mebius-van de Laar, G. de Wind, The combining of sodium chloride and calcium chloride by the hardened portland cement compounds C_3S, C_2S, C_3A and C_4AF, Proc. 7th Int. Symp. on Chemistry of Cement, Paris, 1980, pp. 823–828.

[66] C. Moyne, M.A. Murad, Electro-chemo-mechanical couplings in swelling clays derived from a micro/macro-homogenization procedure, Int. J. Solids Struct. 39 (25) (2002) 6159–6190.

[67] O. Coussy, M. Thiery, M.D. Nguyen, Drying asymptotics, in: H.I. Ling (Ed.), Proc. 4th Biot Conf. on Poromechanics, New York, USA, Materials Science Book from CHIPS, , June 8–10, 2009, pp. 384–390.